Journal of Structural Biology 216 (2024) 108115

Contents lists available at ScienceDirect

Journal of Structural Biology

journal homepage: www.elsevier.com/locate/yjsbi

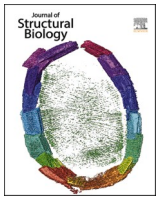

Structure Report

A glimpse into the hidden world of the flexible C-terminal protein binding domains of human RAD52

Lucas R. Struble, Jeffrey J. Lovelace, Gloria E.O. Borgstahl *

The Eppley Institute for Research in Cancer and Allied Diseases, 986805 Nebraska Medical Center, Omaha, NE 68198-6805, USA

ARTICLE INFO

Keywords:
RAD52
Homologous recombination
Single strand annealing
Replication Protein A
RAD51
Small angle X-ray scattering
Cancer therapeutics

ABSTRACT

Human RAD52 protein binds DNA and is involved in genomic stability maintenance and several forms of DNA repair, including homologous recombination and single-strand annealing. Despite its importance, there are very few structural details about the variability of the RAD52 ring size and the RAD52 C-terminal protein–protein interaction domains. Even recent attempts to employ cryogenic electron microscopy (cryoEM) methods on full-length yeast and human RAD52 do not reveal interpretable structures for the C-terminal half that contains the replication protein A (RPA) and RAD51 binding domains. In this study, we employed the monodisperse purification of two RAD52 deletion constructs and small angle X-ray scattering (SAXS) to construct a structural model that includes RAD52's RPA binding domain. This model is of interest to DNA repair specialists as well as for drug development against HR-deficient cancers.

1. Introduction

Human RAD52 is a nonessential DNA/RNA binding protein involved in homologous recombination (HR) double-strand break repair (DSB) in both the gene conversion and single-strand annealing pathways (Balboni et al., 2023). RAD52 is an interesting drug target for breast, ovarian, prostate, and pancreatic cancers because when inactivated, it is synthetically lethal with HR deficiency (Feng et al., 2011; Hanamshet et al., 2016; Lok et al., 2013; Pilarski, 2019). RAD52 is composed of 418 amino acids (Fig. S1 (A)). The N-terminal half binds DNA/RNA and forms a ring structure (Kagawa et al., 2002; Saotome et al., 2018; Singleton et al., 2002), and the flexible C-terminal half contains regions that interact with replication protein A (RPA) and RAD51 protein (Park et al., 1996). Multiple crystal and cryogenic electron microscopy (cryoEM) structures exist for the structured N terminal half (Fig. 1 and Supplementary Fig. S1 (B, C))(Deveryshetty et al., 2023; Kagawa et al., 2002; Kinoshita et al., 2023; Saotome et al., 2018; Singleton et al., 2002). Unfortunately, the flexible C-terminal half has no available structure. Even when the full-length human or yeast protein is used in the purified sample, the C-terminal half can not be visualized by cryoEM. Therefore, there is a need for a structural model for the C-terminal half of RAD52 as the protein–protein interaction regions for RPA and RAD51 are of particular interest as drug targets to exploit RAD52's synthetic lethality (Al-Mugotir et al., 2019; Al-Mugotir et al., 2021).

In this study, SAXS data for two RAD52 constructs were measured: RAD52(1–212) (for which a crystal structure exists) and RAD52(1–303) (which includes the RPA binding domain of RAD52). We did not use full-length RAD52 protein samples for SAXS studies as they are polydisperse and known to have multiple levels of aggregation and so are not useful for SAXS analysis (Ranatunga et al., 2001a; Ranatunga et al., 2001b). We were able to use the derived SAXS molecular envelope for RAD52 (1–212) to orient a model based on the crystal structure and locate the positions of the C-terminal half in solution. Using the I-TASSER server for protein structure prediction (Zhang, 2008), we were able to model what a folded C-terminal "tail" of RAD52(1–303) would look like that is in agreement with the SAXS data. The resulting model provides a higher-resolution view of RAD52 than the low-resolution silver-stained images that showed the C-terminal half of RAD52 hanging down from the N-terminal ring like the tendrils of a jellyfish (Ranatunga et al., 2001b).

2. Materials and methods

2.1. Recombinant protein expression

The His-tagged RAD52(1–212) and RAD52(1–303) pET28a expression plasmids were transformed into Rosetta2 *E. coli* cells using the manufacturer's protocols (Novagen). RAD52(1–212) had a thrombin-cleavable His tag. RAD52(1–303) had a noncleavable C-terminal His

* Corresponding author.
E-mail address: gborgstahl@unmc.edu (G.E.O. Borgstahl).

https://doi.org/10.1016/j.jsb.2024.108115
Received 1 March 2024; Received in revised form 25 July 2024; Accepted 4 August 2024
Available online 6 August 2024

tag. Selection of transformed cells was performed on agarose plates containing 30 μg/ml kanamycin and 34 μg/ml chloramphenicol. A colony was selected and grown in lysogeny broth (LB) media incubated at 37 °C with 170 rpm shaking until it reached an optical density at 600 nm (OD600) between 0.7 and 0.9. Cell cultures were induced with 1 mM isopropyl β-D-1-thiogalactopyranoside (IPTG), cooled to 18 °C, and allowed to shake overnight. Cells were harvested by centrifugation at 14,000 x *g* and stored at −20 °C.

2.2. Protein purification

Cell pellets were suspended in an immobilized metal ion affinity chromatography (IMAC) running buffer (50 mM Tris HCl, pH 7.8, 300 mM KCl, 10 mM imidazole, 10% glycerol, 2 mM 2-mercaptoethanol (BME)) with protease inhibitor cocktail compatible with histidine-tagged proteins (Sigma) added at 250 μl per gram of cells. Bacterial lysis was achieved with 3 passes through an Emulsiflex-C3, and the resulting lysate was centrifuged for 30 min at 40,000 x *g*. The supernatant was filtered using a 0.45 μm HV Durapore^{R} membrane filter (MilliporeSigma). The purification protocol used was a variant of the method described in Kagawa et al., (2002) and Ranatunga et al., (2001) with the following changes. Purification was performed on an ÄKTAPure (Cytiva) using a 5 ml HisTrap FF column (Cytiva). The column was equilibrated with 5 column volumes (CV) of IMAC running buffer, loaded with the protein lysate, washed with 10 CV of IMAC loading buffer, and then eluted with 5 CV steps at 50 mM, 150 mM, and 300 mM imidazole. The protein eluted during the 300 mM step was then pooled and dialyzed against 1 L of heparin running buffer (50 mM Tris-HCl, pH 7.5, 200 mM KCl, 10% Glycerol, 0.5 mM ethylenediaminetetraacetic acid (EDTA)) overnight. Thrombin was added to the dialysis for RAD52 (1–212) samples to cleave the HIS tag. A 5 ml HiTrap Heparin HP (Cytiva) column was equilibrated with 5 CV of heparin running buffer, the dialyzed protein was loaded onto the column, and the column was washed with 10 CV of heparin running buffer. The bound protein was eluted using a 1 M NaCl gradient over 20 CV. The protein peak was pooled and dialyzed overnight against a size exclusion chromatography (SEC) buffer (20 mM Bis-Tris, pH 6.0, 10% glycerol, 400 mM NaCl, 100 mM KCl, 1 mM EDTA). The dialyzed sample was passed through a HiLoad 16/600 Superdex 200 pg column (Cytiva) and collected in 1 ml fractions. Protein concentrations were taken using A_{280} with an extinction coefficient (Ɛ) of 20400. Examination of samples by DLS showed that the R_H of the RAD52 samples did not change significantly with pH, indicating that lowering the pH does not introduce significant artifacts.

2.3. Light scattering

Individual protein fractions were concentrated using a 10 kDa MWCO concentrator (GE Lifesciences) and checked with dynamic light scattering (DLS) for monodispersity using a DynaPro MS/X using Dynamics 6.7.7 software (Wyatt Technology Corporation). Monodisperse samples were combined and examined by size exclusion chromatography with multi-angle light scattering (SEC-MALS) using an Agilent 1260 chromatography system with attached miniDAWN TREOS, Optilab T-rEX, and WTC-050S5 column (Wyatt Technology Corporation). Data collection and processing were performed with ASTRA 6 software (Wyatt Technology Corporation).

2.4. Small angle X-ray scattering (SAXS)

SAXS analysis was performed using a BioSAXS1000 (Rigaku) and FR-E rotating anode X-ray generator ($\lambda = 1.54$ Å). Images were collected for 90 min, with subframes taken every 10 min. No protein damage was observed. Raw images were processed into background subtracted scattering curves with SAXSLab. Scattering curves were further processed and analyzed with the automated analysis pipeline (AAP) in the SAXSLab software running the ATSAS package (Petoukhov et al., 2012)

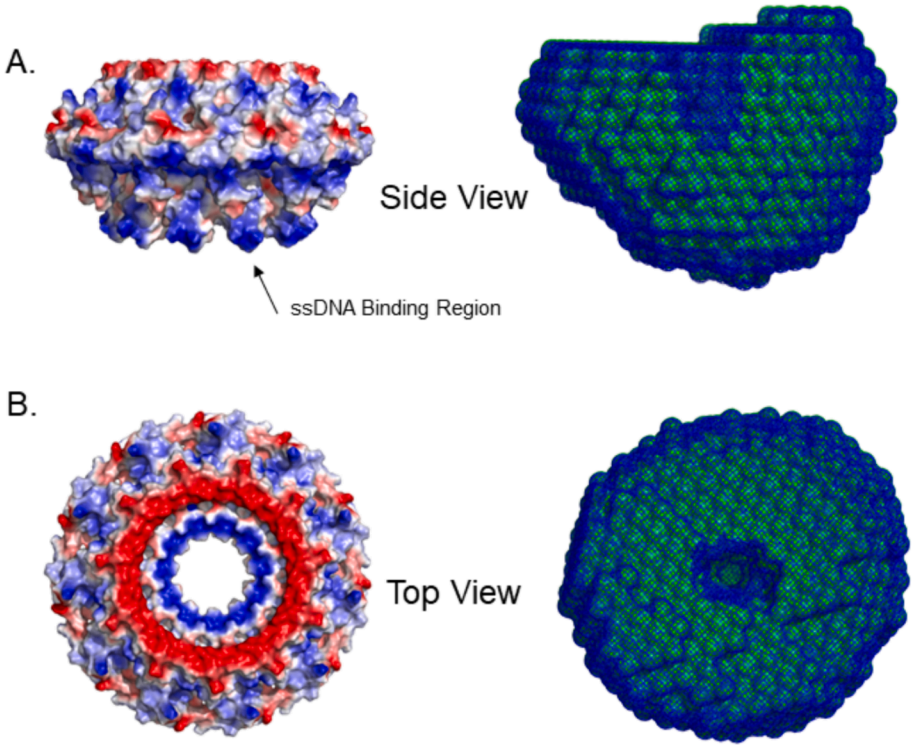

Fig. 1. Comparison of the SAXS *ab initio* model of RAD52(1–212) with the published RAD52(1–212) structure (1kn0) electrostatic surface. RAD52(1–212) viewed from the (A) side and (B) top. The electrostatic surface model of 1kn0 (left) is shown next to the SAXS *ab initio* model of RAD52(1–212) (right, green). A blue wireframe model has been superimposed over the bead model to highlight the central cavity. Interestingly, we expected the SAXS surface to look like a donut with a hole, but instead, it resembled a raspberry.

and BioXTAS RAW (Hopkins, 2024). Docking of models with SAXS envelopes was done with the Situs package using the Colores program (Chacon and Wriggers, 2002; Wriggers, 2010). Figures were made using PyMol (Schrödinger, LLC).

3. Results and discussion

3.1. Sample preparation

The quality of this study was reliant on the purification of monodisperse RAD52 samples. Both RAD52(1–212) and RAD52(1–303) showed elution peaks at 150 mM and 300 mM imidazole, but we found that the 300 mM imidazole elution displayed lower polydispersity in downstream tests, so only the 300 mM imidazole fractions were used for these experiments. DLS showed both RAD52(1–212) and RAD52(1–303) samples to be monodisperse, with a polydispersity of 12.2 % and 14 %, respectively (Supplementary Fig. S2). SEC-MALS of the same fractions showed RAD52(1–212) as monodisperse with a molecular weight (MW) of 229 kDa, and given that the calculated monomer MW is 23.7 kDa this shows that the RAD52(1–212) ring was composed of 9.7 subunits (Supplementary Fig. S3). SEC-MALS of RAD52(1–303) showed that the protein sample was also monodisperse but with a slight increase in MW as the peak eluted (Supplementary Fig. S3). The MW begins at 320 kDa and rises to 349 kDa across the peak, giving an overall MW 328.7 kDa. Given that the calculated monomer MW is 34.6 kDa, this indicated that the RAD52(1–303) ring is composed of 9.5 subunits on average.

3.2. SAXS of RAD52(1–212)

The first step in our analysis was the acquisition of a SAXS envelope of a RAD52 sample with a known crystal structure, RAD52(1–212). RAD52(1–212) at a concentration of 7.48 mg/ml was found to provide the best scattering data and envelope. The Guinier plot showed no evidence of aggregation, the Kratky plot showed a well-folded, globular multidomain protein, and the P(r) plot showed a maximum dimension of 117.7 Å (Supplementary Fig. S4). *Ab initio* bead modeling shows the SAXS envelope for Rad52(1–212) looks like a partially hollow, raspberry shaped, half-sphere with a diameter of 120 Å (Fig. 1). A decameric model of RAD52(1–212) was created using CNS SOLVE from an available crystal structure (PDB ID 1kn0; Fig. 2A). and docked with the SAXS envelope using the Colores program, where the best orientation was found to be with the DNA binding region of RAD52(1–212) residing in the curved portion of the half-sphere (Fig. 2B)(Kagawa et al., 2002; Saotome et al., 2018).

3.3. SAXS of RAD52(1–303)

SAXS data for the RAD52(1–303) sample was then collected. The concentration tested was 7.11 mg/ml. No signs of aggregation were seen with the Guinier plot; the Kratky plot shows a globular multidomain protein with flexible linker regions, and the P(r) plot showed a maximum dimension of 181.0 Å (Supplementary Fig. S5). *Ab initio* bead modeling shows the SAXS envelope as pear-shaped with an end-to-end length of 174 Å and the wider region having a diameter of approximately 120 Å (Fig. 3(A)). The curved top of the wider region is almost

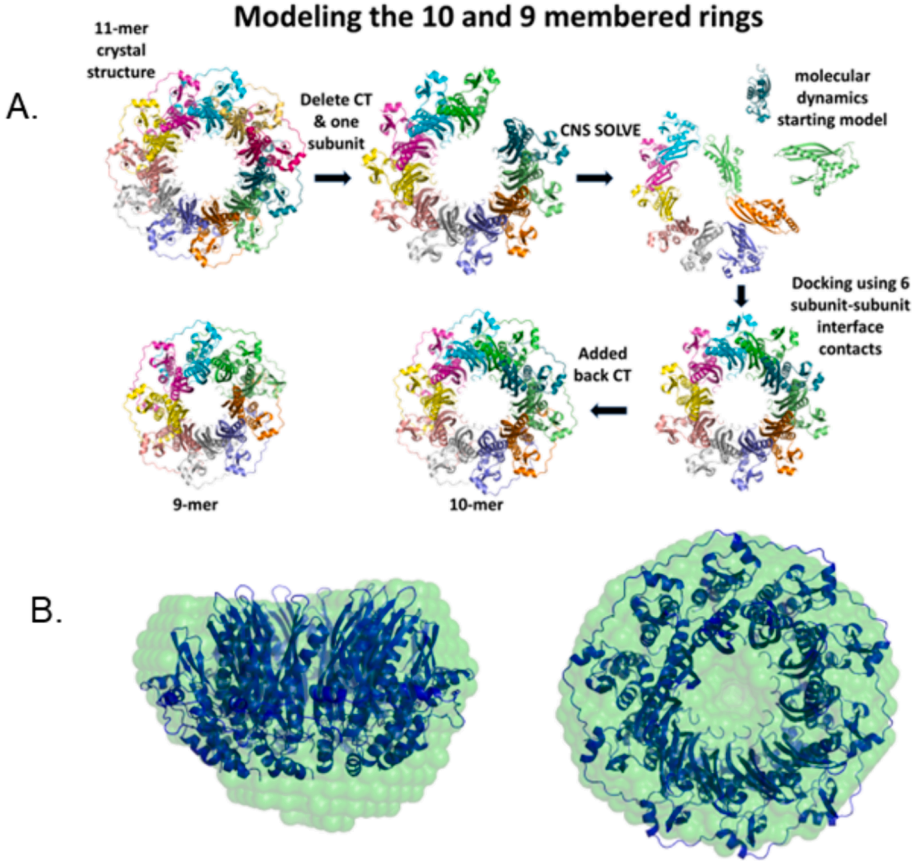

Fig. 2. Creation of the RAD52(1–212) decameric model and subsequent docking with the SAXS envelope. (A) The decameric model of RAD52 was created by first removing a subunit from the undecameric crystal structure. Then, the C-terminal peptide (residues 177–209) that wraps around the adjacent subunit was temporarily deleted. CNS SOLVE was then used to perform molecular dynamics with six interface contacts acting as restraints, resulting in a model for a decameric ring. The C-terminal peptide was then returned to the model by superposition. (B) The decameric model was docked with the SAXS envelope using Colores, and the DNA binding region of RAD52 was found to align with the rounded dome.

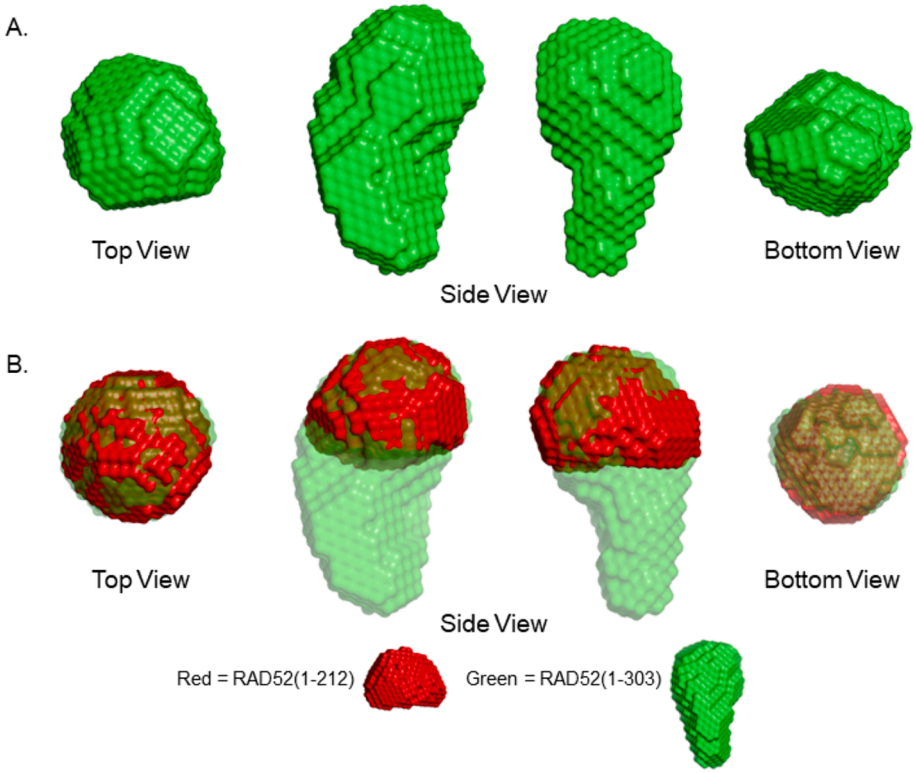

Fig. 3. The SAXS *ab initio* model of RAD52(1–303) and docking of RAD52(1–212) SAX envelope. (A) A view of the RAD52(1–303) SAXS envelope from the largest diameter region down (Top View), from two different angles at the side (Side View), and from the narrowest portion looking upward (Bottom View). The molecule is 174 Å top to bottom (Side View) and 120 Å in diameter at the largest diameter region (Top View). (B) Docking of the SAXS envelopes for RAD52(1–212) and RAD52 (1–303). The curved face of the RAD52(1–212) SAXS envelope (red) to the larger domed region of RAD52(1–303) (green), showing the alignment of the RAD52 (1–303) molecule. With this, it can be extrapolated that the DNA binding domain of RAD52(1–212) orients toward the top of this dome, with the C-terminal region oriented into the narrow lower portion of the envelope.

identical to the curve for the Rad52(1–212) half sphere. This provided a common orientation for both structures and indicates that the likely placement of the RAD52(1–303) ring is with the DNA binding region facing the rounded end of the wider region. As SEC-MALS showed that RAD52(1–303) is likely a nonamer, a nonameric model was created in the same fashion as the decameric model (Fig. 2A) and docked with the RAD52(1–303) SAXS envelope in the location and orientation indicated by the placement of the RAD52(1–212) envelope and docked decameric

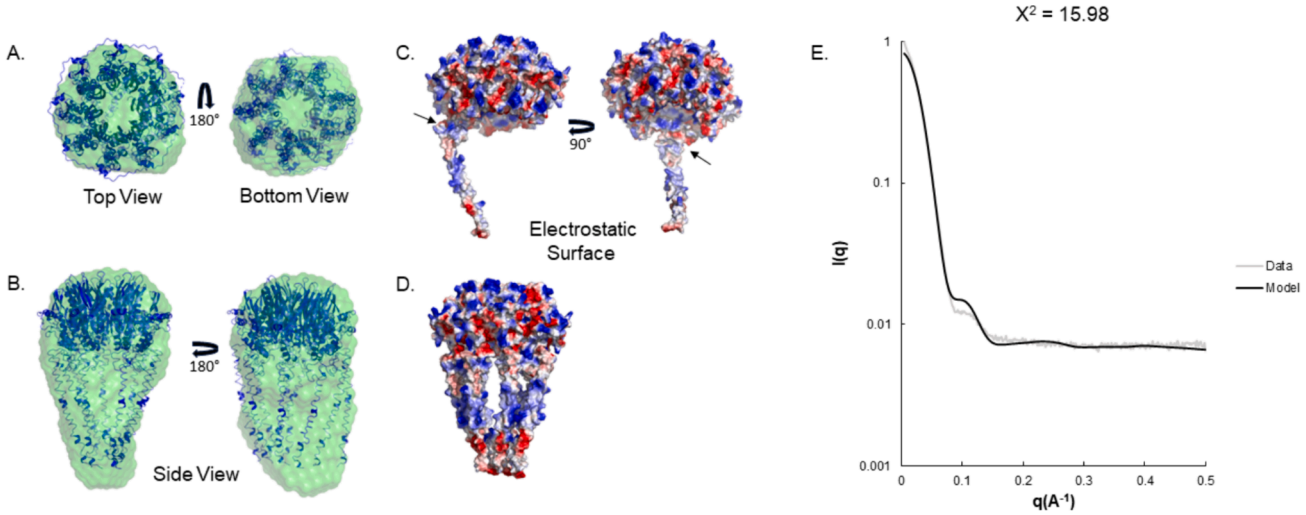

Fig. 4. I-TASSER folded (213–303) attached to RAD52(1–212) nonamer. Nonameric RAD52(1–212) with attached I-TASSER folded 213–303 amino acids (blue) docked inside the RAD52(1–303) SAXS envelope (green). Shown is the model seen from the top and bottom (A), the side with a 180° turn (B), the electrostatic surface map of the RAD52(1–212) nonamer with a single (213–303) C-terminus modeled (C) and rotated 90°, and the RAD52(1–212) nonamer with all (213–303) C-termini modeled (D). The ribbon model of the RAD52(1–212) nonamer with all C-terminal (213–303) amino acids on each subunit fits well inside the RAD52(1–303) SAXS envelope. In the electrostatic surface model, blue represents positively charged regions and red represents negatively charged regions. The region of RAD52 which interacts with RPA is indicated with a small arrow, and is known to be positively charged to interact with RPA's negatively charged interaction domain. This atomic model (E, black) was fit against the experimental scattering curve (E, grey), analysis with Crysol yields a χ^2 value of 15.98 between the data sets.

model (Fig. 3(B)). The missing amino acids (213–303), when fully extended, reach far outside of the RAD2(1–303) SAXS envelope, implying that the C-terminal region must be folded (Supplementary Fig. S6). These amino acids that were missing from the RAD52(1–212) structure were modeled using I-TASSER (Roy et al., 2010; Yang and Zhang, 2015; Zhang, 2008). The model of the now-folded 91 amino acids was manually docked to a RAD52(1–303) subunit (Fig. 4). This modeled C-terminal tail matches the contours of the RAD52(1–303) SAXS envelope quite well (Fig. 4AB). The quality of the model for residues 213–303 is shown in the ramachandran plot (Fig. S7). The N-terminal 213 to 245 residues are folded into a globular domain with an alpha helix starting at Gln237. Then a coil of right (green) and left handed (blue) helical turns comprise the remaining structure. Throughout, secondary structural elements are broken up by proline residues. The electrostatic surface of the model (Fig. 4CD) shows how the charged surface is on the exterior and the more neutral surface is on the inside of the nonamer. These complementary surface interactions help hold the monomer together for the C-terminal tails to hang down from the N-terminal ring.

This fully assembled nonamer atomic model was fit against the experimental scattering curve using Crysol (Curtis et al., 2012; Svergun et al., 1995) and had a decent fit with a χ^2 (Svergun et al., 1995)value of 15.98. The SECMALS data had some disagreement about the number of subunits in the ring for the 1–303 construct so a decamer model was also constructed and studied as well as variation with the arms swung outward (Figure S8). All iterations had worse χ^2 than the nonamer model. Additionally, a mixture of nonamer and decamers was analyzed in excel using the evolutionary solver to minimize the χ^2. By adjusting the ratio of the nonamer to decamer model. The result was always 100% nonamer model for the lowest χ^2. The scattering curves for the decamer model showed variation in the q region from 0.08 to 0.2 (Figure S8) which corresponds to the region where the nonamer differs from the scattering data the most but it seems to capture the overall trends observed in the region.

3.4. Variability of the RAD52 ring size

Previously published methods for purifying RAD52(1–212) produced pure and monodisperse protein, and the crystal structure for RAD52(1–212) shows the protein forming an undecameric ring. For our experiments, we transitioned these earlier methods to one more appropriate for SAXS analysis. We lowered the pH of the previously published RAD52 SEC buffer to be further from the protein's isoelectric point to promote solubility and increased salt concentrations to protect against aggregation caused by X-ray exposure. DLS control experiments showed that lowering the pH did not significantly change the ring size. Once purified to a quality compatible with SAXS, our RAD52(1–212) showed a shift from the crystal structures undecameric ring to a mixture of a majority of decameric rings with a few nonameric rings as shown by our SEC-MALS data, indicating 229 kDa average MW, equaling 9.7 subunits (Supplementary Fig. S3). In reflection of this, we used the undecameric crystal structure as a template to create a decameric model. The undecameric crystal structure and decameric model were both docked with the SAXS envelope for RAD52(1–212), and we found that the undecameric model would not fit inside the SAXS envelope without a significant portion of the structure extending outside. The decameric model fits much better, and the best orientation was with the DNA binding region of the RAD52(1–212) ring facing the curved region of the SAX envelope. RAD52(1–303) was purified in the same manner as RAD52(1–212). We found that not all fractions from SEC were monodisperse. We believe this is because SEC was separating the RAD52 rings into nonamers and decamers. The most monodisperse fractions were used for SEC-MALS, where we determined an average MW of 328.7 kDa, indicating an average of 9.5 RAD52(1–303) subunits (Supplementary Fig. S3). During elution from SECMALS, the MW line increases over time indicating that the sample was made of a mixture of nonamers and decamers. The exact number of subunits in the RAD52 ring may not be physiologically relevant, as experimentally it varies. We were unable to perform these experiments with wild-type RAD52 due to its polydispersity and so we don't know how many subunits are in the ring using DLS or SAXS methods.

3.5. Putative structure of RAD52 C-terminal RPA interaction domain

Both SAXS envelopes have an almost identical curved dome section. We aligned these portions and used this positioning to determine the orientation of the RAD52(1–303) nonameric model. To represent the RAD52(1–303) amino acids not present in the RAD52(1–212) model, the sequence for RAD52(213–303) was modeled by I-TASSER and added to the RAD52(1–303) nonameric model. The most likely conformation had a Z score of 1.14 and a C score of −2.77. These modeled amino acids fit quite well into the RAD52(1–303) SAXS envelope. Alphafold was unable to fold the RAD52(213–303) peptide. Although it is a powerful tool for exploring protein folding, Alphafold is reliant on searching for existing structures with sequence homology when generating models (Jumper et al., 2021). I-TASSER also uses protein sequences to look for structural homology, but it also puts those models through a protein function database that checks into relevant ligand–protein binding interactions. This additional step from I-TASSER takes the extended random coil shown in other folding programs and shows a folded model for the RAD52 C-terminal amino acids. In this model, amino acids (213–250) fold into a positively charged domain nested near the main RAD52 (1–212) molecule on the side opposite the DNA binding domain (Fig. 4). We find this significant as a well-known RAD52 binding partner, RPA, binds in this region. RPA interacts with RAD52 through a negatively charged domain (Jackson et al., 2002). Interestingly, the I-TASSER model has a positively charged surface in the RAD52(221–280) RPA binding region (Supplementary Fig. S1). In conclusion, the SAXS analysis combined with crystal structures and molecular modeling provides a glimpse into what, up until now, has been a hidden world of protein–protein interactions contained within the flexible C-terminal half of RAD52. This structural information can be used in the development of RAD52 targeting therapeutics.

CRediT authorship contribution statement

Lucas R. Struble: Writing – review & editing, Writing – original draft, Visualization, Methodology, Investigation, Formal analysis, Data curation. **Jeffrey J. Lovelace:** Writing – review & editing, Visualization, Validation, Software, Methodology, Investigation. **Gloria E.O. Borgstahl:** Writing – review & editing, Supervision, Funding acquisition, Conceptualization.

Declaration of competing interest

The authors declare that they have no known competing financial interests or personal relationships that could have appeared to influence the work reported in this paper.

Data availability

The SAXS data and models were deposited in the Small Angle Scattering Biological Data Bank (sasbdb.org) with IDs SAS5677 and SAS5645.

Acknowledgements

We thank Dr. Gilson Baia for creating the RAD52(1-212) expression plasmid and Dr. Min Park at Los Alamos National Laboratory for the RAD52(1-303) expression plasmid.

Funding

The research was supported by the Fred & Pamela Buffett Cancer Center Support Grant (P30CA036727) pilot project funding, the Nebraska Research Initiative for the purchase of the SAXS instrument, and research funding from the Nebraska Department of Health and Human Services. LRS also acknowledges the U.S. Department of Education GAANN (P200A120231) and Nebraska NASA EPSCoR Space Grant for student fellowships.

Appendix A. Supplementary data

Supplementary data to this article can be found online at https://doi.org/10.1016/j.jsb.2024.108115.

References

Al-Mugotir, M., Kolar, C., Vance, K., Kelly, D.L., Natarajan, A., Borgstahl, G.E.O., 2019. A simple fluorescent assay for the discovery of protein-protein interaction inhibitors. Anal. Biochem. 569, 46–52.

Al-Mugotir, M., Lovelace, J.J., George, J., Bessho, M., Pal, D., Struble, L., Kolar, C., Rana, S., Natarajan, A., Bessho, T., Borgstahl, G.E.O., 2021. Selective killing of homologous recombination-deficient cancer cell lines by inhibitors of the RPA: RAD52 protein-protein interaction. PLoS One 16, e0248941.

Balboni, B., Rinaldi, F., Previtali, V., Ciamarone, A., Girotto, S., Cavalli, A., 2023. Novel insights into RAD52's structure, function, and druggability for synthetic lethality and innovative anticancer therapies. Cancers (Basel) 15.

Chacon, P., Wriggers, W., 2002. Multi-resolution contour-based fitting of macromolecular structures. J. Mol. Biol. 317, 375–384.

Curtis, J.E., Raghunandan, S., Nanda, H., Krueger, S., 2012. SASSIE: A program to study intrinsically disordered biological molecules and macromolecular ensembles using experimental scattering restraints. Comput. Phys. Commun. 183, 382–389.

Deveryshetty, J., Chadda, R., Mattice, J.R., Karunakaran, S., Rau, M.J., Basore, K., Pokhrel, N., Englander, N., Fitzpatrick, J.A.J., Bothner, B., Antony, E., 2023. Yeast Rad52 is a homodecamer and possesses BRCA2-like bipartite Rad51 binding modes. Nat. Commun. 14, 6215.

Feng, Z., Scott, S.P., Bussen, W., Sharma, G.G., Guo, G., Pandita, T.K., Powell, S.N., 2011. Rad52 inactivation is synthetically lethal with BRCA2 deficiency. Proc. Natl. Acad. Sci. USA 108, 686–691.

Hanamshet, K., Mazina, O.M., Mazin, A.V., 2016. Reappearance from obscurity: mammalian Rad52 in homologous recombination. Genes (Basel) 7.

Hopkins, J.B., 2024. BioXTAS RAW 2: new developments for a free open-source program for small-angle scattering data reduction and analysis. J. Appl. Cryst. 57, 194–208.

Jackson, D., Dhar, K., Wahl, J.K., Wold, M.S., Borgstahl, G.E., 2002. Analysis of the human replication protein A:Rad52 complex: evidence for crosstalk between RPA32, RPA70, Rad52 and DNA. J. Mol. Biol. 321, 133–148.

Jumper, J., Evans, R., Pritzel, A., Green, T., Figurnov, M., Ronneberger, O., Tunyasuvunakool, K., Bates, R., Zidek, A., Potapenko, A., Bridgland, A., Meyer, C., Kohl, S.A.A., Ballard, A.J., Cowie, A., Romera-Paredes, B., Nikolov, S., Jain, R., Adler, J., Back, T., Petersen, S., Reiman, D., Clancy, E., Zielinski, M., Steinegger, M., Pacholska, M., Berghammer, T., Bodenstein, S., Silver, D., Vinyals, O., Senior, A.W., Kavukcuoglu, K., Kohli, P., Hassabis, D., 2021. Highly accurate protein structure prediction with AlphaFold. Nature 596, 583–589.

Kagawa, W., Kurumizaka, H., Ishitani, R., Fukai, S., Nureki, O., Shibata, T., Yokoyama, S., 2002. Crystal structure of the homologous-pairing domain from the human Rad52 recombinase in the undecameric form. Mol. Cell 10, 359–371.

Kinoshita, C., Takizawa, Y., Saotome, M., Ogino, S., Kurumizaka, H., Kagawa, W., 2023. The cryo-EM structure of full-length RAD52 protein contains an undecameric ring. FEBS Open Bio 13, 408–418.

Lok, B.H., Carley, A.C., Tchang, B., Powell, S.N., 2013. RAD52 inactivation is synthetically lethal with deficiencies in BRCA1 and PALB2 in addition to BRCA2 through RAD51-mediated homologous recombination. Oncogene 32, 3552–3558.

Park, M.S., Ludwig, D.L., Stigger, E., Lee, S.H., 1996. Physical interaction between human RAD52 and RPA is required for homologous recombination in mammalian cells. J. Biol. Chem. 271, 18996–19000.

Petoukhov, M.V., Franke, D., Shkumatov, A.V., Tria, G., Kikhney, A.G., Gajda, M., Gorba, C., Mertens, H.D., Konarev, P.V., Svergun, D.I., 2012. New developments in the ATSAS program package for small-angle scattering data analysis. J. Appl. Cryst. 45, 342–350.

Pilarski, R., 2019. The role of BRCA testing in hereditary pancreatic and prostate cancer families. Am. Soc. Clin. Oncol. Educ. Book 39, 79–86.

Ranatunga, W., Jackson, D., Flowers 2nd, I.R., Borgstahl, G.E., 2001a. Human RAD52 protein has extreme thermal stability. Biochemistry 40, 8557–8562.

Ranatunga, W., Jackson, D., Lloyd, J.A., Forget, A.L., Knight, K.L., Borgstahl, G.E., 2001b. Human RAD52 exhibits two modes of self-association. J. Biol. Chem. 276, 15876–15880.

Roy, A., Kucukural, A., Zhang, Y., 2010. I-TASSER: a unified platform for automated protein structure and function prediction. Nat. Protoc. 5, 725–738.

Saotome, M., Saito, K., Yasuda, T., Ohtomo, H., Sugiyama, S., Nishimura, Y., Kurumizaka, H., Kagawa, W., 2018. Structural basis of homology-directed DNA repair mediated by RAD52. iScience 3, 50–62.

Singleton, M.R., Wentzell, L.M., Liu, Y., West, S.C., Wigley, D.B., 2002. Structure of the single-strand annealing domain of human RAD52 protein. Proc. Natl. Acad. Sci. USA 99, 13492–13497.

Svergun, D., Barberato, C., Koch, M.H.J., 1995. CRYSOL - a program to evaluate X-ray solution scattering of biological macromolecules from atomic coordinates. J. Appl. Cryst. 28, 768–773.

Wriggers, W., 2010. Using Situs for the integration of multi-resolution structures. Biophys. Rev. 2, 21–27.

Yang, J., Zhang, Y., 2015. Protein structure and function prediction using I-TASSER. Curr. Protoc. Bioinformatics 52, 1–5.

Zhang, Y., 2008. I-TASSER server for protein 3D structure prediction. BMC Bioinf. 9, 40.